Korean J. Chem. Eng., 32(9), 1766-1773 (2015)
DOI: 10.1007/s11814-015-0031-0

pISSN: 0256-1115
eISSN: 1975-7220

High performance of manganese oxide octahedral molecular sieve adsorbents for removing sulfur compounds from fuel gas

Phuoc Hoang Ho*, Seong Chan Lee*, Jieun Kim, Doohwan Lee**,†, and Hee Chul Woo*,†**

*Department of Chemical Engineering, Pukyong National University, San 100, Yongdang-dong, Nam-gu, Busan 608-739, Korea
**Department of Chemical Engineering, The University of Seoul, 13 Siripdae-gil, Dongdaemun-gu, Seoul 130-743, Korea
(*Received 3 December 2014 • accepted 5 February 2015*)

Abstract−Properties of porous manganese oxide adsorbents for adsorptive removal of *tert*-butylmercaptan (TBM) from CH_4 fuel gas were investigated at ambient temperature and atmospheric pressure. The adsorbents were prepared by oxidation reactions of Mn^{2+} with $KMnO_4$ and via the sol-gel method by reduction of $KMnO_4$ using fumaric acid as the reducing agent. The effects of preparation method, precursor, temperature, and time for the structure and desulfurization properties of the resulting adsorbents were studied. Cryptomelane octahedral manganese oxide molecular sieve (OMS-2) adsorbents exhibited high breakthrough TBM adsorption (1.3-2.5 mmol g^{-1}) with the properties varied by the synthesis condition. The OMS-2-Ac prepared by the oxidation reactions of manganese acetate resulted in smaller OMS-2 crystallites with higher surface area compared to those prepared from manganese sulfate and chloride precursors, and it exhibited an enhanced TBM adsorption uptake. TBM adsorption capacity of OMS-2 could be further enhanced by introducing Cu into the structure. This gave rise to a markedly high TBM breakthrough adsorption (7.4 mmol g^{-1}) for Cu-OMS-2 (7.8 wt% Cu doping), which is significantly greater than the values reported for activated carbon, zeolite, and other porous oxide based solid adsorbents at similar conditions in the literature.

Keywords: Adsorptive Desulfurization, Manganese Oxide Molecular Sieve, Tert-Butylmercaptan, Fuel Processing, Fuel Cell

INTRODUCTION

Selective removal of organosulfur compounds from gaseous hydrocarbon fuels, such as thiophenes, thiols, and sulfides that are commonly used as odorants for warning of fuel leakage, is a significant fuel processing step for clean hydrogen production for polymer electrolyte membrane fuel cell (PEMFC) [1-3]. The presence of such organosulfur species even in minute concentrations (ppm) can result in a gradual and significant degradation of the fuel processing catalysts and Pt-based electrodes by irreversible poisoning [4,5]. Adsorptive removal of organosulfur species at ambient temperatures is considered an effective and viable fuel desulfurization method for fuel cells, because it is a significantly simpler than the conventional catalytic hydrodesulfurization (HDS) process [6]. Various solid adsorbents, including activated carbons [3,7-9], zeolites [2, 10-17], and porous metal oxides [18-20], have been studied for this purpose. In general, these studies demonstrated that adsorptive desulfurization properties of the solid adsorbents could be enhanced by various modifications such as modulation of surface acid-base characteristics, incorporation of metal ions or clusters of high sulfur adsorption affinities, and variation of pore structure and material properties.

We recently reported the unique adsorptive desulfurization properties of cryptomelane manganese oxide octahedral molecular sieves (OMS-2) in gaseous hydrocarbon fuels [21]. OMS-2 exhibited unprecedented high breakthrough adsorption capacity and selectivity for *tert*-butylmercaptan (TBM) at ambient temperature and atmospheric pressure in the presence of tetrahydrothiophene (THT) and dimethyl sulfide (DMS). The results were largely different from those previously reported for activated carbon and zeolite based adsorbents, considering that TBM usually showed weaker adsorption than THT and DMS on these previously studied porous solids. OMS-2 has one-dimensional pore structure with primary MnO_6 octahedral building units linked at their edges and vertexes to form 2×2 square tunnels with the pore size approximately 0.46 nm×0.46 nm [22]. It has a composition of $KMn_8O_{16}{\cdot}nH_2O$ with the potassium cation K^+ placed inside the tunnel for charge balancing [23]. The co-presence of Mn^{+2}, Mn^{+3}, and Mn^{+4} ions in the framework yields an average oxidation state of ~3.8 for Mn, and the balancing K^+ can be exchanged with other metal cations [22-25]. OMS-2 based materials have been recently studied for uses such as oxidative catalysts [26-29], electrodes [30], battery materials [31], and adsorbents [32].

In this work, we investigated adsorptive desulfurization properties of porous manganese oxides prepared via different synthetic routes: (i) oxidation of Mn^{2+} in aqueous acid using $KMnO_4$ reagent, (ii) sol-gel based reaction between $KMnO_4$ and fumaric acid. The preparation method, manganese precursor, synthesis temperature, and time had significant effects on the physicochemical and desulfurization properties of the resulting manganese oxide adsorbents. In addition, the TBM uptake amount on OMS-2 could be increased with an increase in the amount of Cu doped into the structure,

†To whom correspondence should be addressed.
E-mail: dolee@uos.ac.kr, woohc@pknu.ac.kr

indicating significant additional roles of Cu for the selective adsorption of TBM. Cu-OMS-2 (7.8 wt% Cu) exhibited a considerably high breakthrough TBM adsorption of 7.4 mmol-S g^{-1}, which was much higher than those previously reported for activated carbon and zeolite based porous solid adsorbents.

EXPERIMENTAL

1. Synthesis of OMS-2 Adsorbents

OMS-2 adsorbents were hydrothermally prepared with modifications of a method reported in the literature varying manganese precursor, hydrothermal temperature, and time [22]. Typically, an aqueous Mn^{2+} solution was prepared by dissolving 26 mmol of a manganese precursor ($MnSO_4$, $MnCl_2$, $Mn(CH_3COO)_2$, or $Mn(HCOO)_2$) in a mixture of 20 ml deionized water and 1.5 ml concentrated HNO_3. These Mn precursors were purchased from Aldrich and used without further purification. A separate aqueous permanganate solution was prepared by dissolving 18.4 mmol $KMnO_4$ (≥99%, Aldrich) in 40 mL deionized H_2O and was then added dropwise iinto the Mn^{2+} precursor solution with vigorous stirring. The mixture was transferred to a Teflon-lined stainless steel autoclave and then placed in an electric oven at 373 K for 24 h. The resulting black precipitates were centrifuged and washed three times with copious amounts of deionized H_2O. The solid samples were dried at 383 K for 12 h and calcined at 723 K for 2 h in air. The resulting OMS-2 samples prepared with manganese-sulfate, -chloride, -acetate, and -formate precursors were designated OMS-2-Sf, OMS-2-Cl, OMS-2-Ac, OMS-2-Fm, respectively. In addition, OMS-2-Ac samples were prepared at various temperatures (313-453 K) and times (0.5-48 h) to investigate the effects of hydrothermal conditions. In a different synthetic route, OMS-2 was prepared by a sol-gel method utilizing $KMnO_4$ and fumaric acid according to the method reported by Ching et al. [33]. The resulting sample was denoted OMS-2-Sg. In addition, copper doped OMS-2, denoted Cu-OMS-2, was also prepared by the same procedure utilizing a mixture of aqueous solutions of manganese acetate and copper acetate with varying amounts of copper in the precursor solution. The resulting Cu-OMS-2 samples were dried at 383 K for 12 h and calcined at 723 K for 2 h in air.

2. Characterizations

Powder X-ray diffraction (XRD) patterns were obtained with graphite-monochromatized Cu K_α radiation operated at 40 kV and 30 mA (X'pert-MPD, Philips). The spectra were taken in the 2θ range from 5 to 80° with a scanning rate of 4° min^{-1}. The structure and morphology of the samples were characterized by field emission scanning electron microscopy (FE-SEM, JSM-7500F, JEOL) and transmission electron microscopy (TEM, JEM-2100, JEOL). The atomic compositions of the samples were obtained using inductively coupled plasma - atomic emission spectrometry (ICP-AES, ICPE-9000, Shimadzu). Thermogravimetric analysis (TGA, TGA7-Pyris-1, Perkin-Elmer) was conducted by raising the temperature from 323 to 1,173 K (ramping rate=10 K min^{-1}) in N_2 atmosphere to investigate the thermal properties of the samples. BET surface areas were determined from N_2 adsorption-desorption isotherms obtained in a volumetric apparatus (BELSORP-MAX, BEL Japan) at 77 K. The oxidation states of the manganese and copper species in the OMS-2 and Cu-OMS-2 were characterized by X-ray photoelectron spectroscopy (XPS, MultiLab 2000, Thermo Scientific).

3. TBM Adsorption Measurement

Adsorption uptake and selectivity of TBM on the adsorbents were obtained in a fixed-bed glass reactor (8 mm I.D.) packed with 100 mg of the adsorbent (particle size 160-225 μm) at 303 K and atmospheric pressure. The TBM uptake measurement and subsequent regeneration of the adsorbents proceeded in three sequential steps: pretreatment, TBM adsorption, and thermal regeneration of the sample. In the pretreatment step, the sample was treated at 723 K for 2 h in flowing He (99.999%) and then naturally cooled to 303 K under the He atmosphere. In the TBM adsorption measurement step, a gaseous mixture containing 100 ppm TBM in CH_4 (certified) was introduced into the reactor at a flow rate of 50 ml min^{-1}. The effluent sulfur concentration was analyzed online with a gas chromatograph (HP 5890 II) equipped with a capillary column (HP-1, 30 m - 0.32 mm - 0.25 μm) and a flame ionization detector (FID). The breakthrough TBM adsorption capacity of an adsorbent is defined as the amount of TBM adsorbed on the sample before its detection in the effluent (the detection limit of FID determined to be ~0.1 ppm). This was calculated from the inlet concentration of sulfur (C_o), inlet flow rate (Q), breakthrough time t (min), and mass of adsorbent m_{ads} (g) according to the following equation:

$$S\ (\text{mmol g}^{-1}) = \frac{q\ (\text{ml min}^{-1}) \times t\ (\text{min}) \times C_{i,o}\ (\text{ppm}) \times 10^{-6}}{22.4\ (\text{ml mmol}^{-1}) \times m_{ads}\ (\text{g})}$$

After saturation of the adsorbent with the sulfur, thermal regeneration of the adsorbent was conducted by temperature programmed desorption (TPD) of the adsorbed sulfur species. The sample was purged in flowing He (50 ml min^{-1}) at 303 K for 1 h, and the temperature was raised to 773 K at a ramping rate of 10 K min^{-1}.

RESULTS AND DISCUSSION

1. Effects of Manganese Precursor and Synthesis Method for OMS-2

The manganese (II) precursors of different anionic salt forms (sulfate, chloride, acetate, and formate) utilized for the preparation of cryptomelane OMS-2 had considerable effects on the resulting structure, morphology, and TBM adsorption properties. This hydrothermal preparation method involves oxidation of Mn^{2+} in aqueous acid in the presence of strong $KMnO_4$ reagent. The properties of these samples were largely different from the OMS-2 obtained by a sol-gel route via reduction of $KMnO_4$ by fumaric acid. Fig. 1 shows the XRD patterns of the samples prepared by different methods and manganese precursors; a reference diffraction pattern of cryptomelane OMS-2 is displayed with a JCPDS number for comparison. The results indicate formation of typical cryptomelane OMS-2 crystal structure on the samples prepared by the Mn^{2+} oxidation using (a) $MnSO_4$ (b) $MnCl_2$, and (c) $Mn(CH_3COO)_2$ precursors. Utilization of (e) $Mn(HCOO)_2$ resulted in the formation of pyrolusite MnO_2, which has a small pore dimension (0.23×0.23 nm [34]) inaccessible to TBM and other larger organosulfur species. The OMS-2 crystal structure was also observed on the sample prepared by the sol-gel method. These XRD results did not show

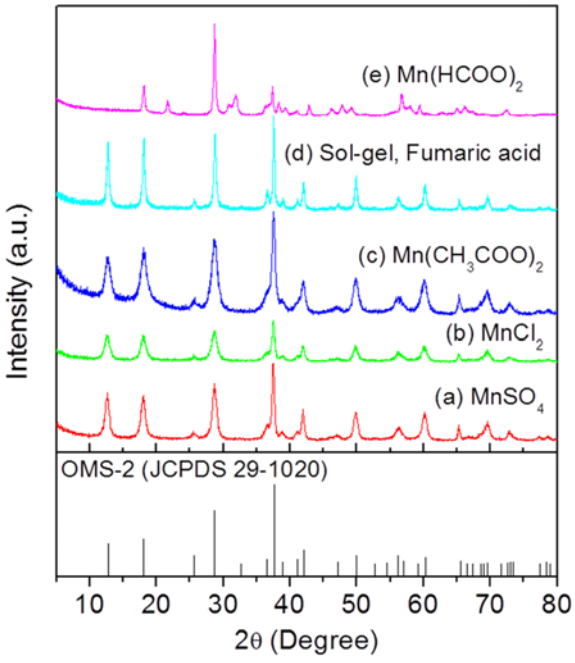

Fig. 1. XRD pattern of porous manganese oxide adsorbents prepared by different synthesis methods and precursors. Sample (a), (b), (c), (e): oxidation of Mn^{2+} by $KMnO_4$ using different Mn precursors; sample (d): sol-gel reaction with reduction of $KMnO_4$ by fumaric acid.

any additional formation of other crystal phases on the samples.

Fig. 2 shows FE-SEM (a)-(d) and TEM (a1)-(d1) micrographs of OMS-2 samples prepared using different synthetic methods and precursors. The results revealed typical needle-like crystalline morphology of OMS-2 on OMS-2-Sf (a), (a1), OMS-2-Cl (b), (b1), and OMS-2-Ac (c), (c1) in which OMS-2 crystallites a few micrometers in length were clustered into bundles. Crystallite size increased in the order shown: OMS-2-Ac<OMS-2-Sf<OMS-2-Cl. OMS-2-Sg prepared by the sol-gel method displayed a different morphology with non-uniform large crystallites and irregular shapes. Table 1 displays elemental composition, average crystal size, and BET surface area of the samples. The average crystal sizes estimated from the XRD results by the Debye-Scherrer method were in agreement with the SEM and TEM results, confirming relatively larger crystals of OMS-2-Sg followed by OMS-2-Sf, OMS-2-Cl, and OMS-2-Ac. Elemental composition and BET surface area results also indicated that the sample prepared using the manganese formate precursor (MnO_2-Fm) was different from OMS-2 with a completely different composition and surface area. The results suggest that OMS-2 crystal growth rate and its formation selectivity were attributed largely to the type of manganese precursors.

Fig. 3 shows TGA analysis results for the manganese oxide samples. The results demonstrated that (a) OMS-2-Sf, (b) OMS-2-Cl, (c) OMS-2-Ac, and (d) OMS-2-Sg exhibited similar thermally induced weight loss characteristics between 323 and 1,173 K. The MnO_2-Fm sample displayed a different weight loss characteristic with a higher thermal stability. Collectively, three characteristic major weight losses of OMS-2 samples were observed in the range of 323-473 K, 673-873 K, and 973-1,073 K, respectively. The weight loss at 323-473 K was due to desorption of physisorbed water, and the loss at 673-873 K was attributed to the removal of chemisorbed oxygen and water from the surface. The weight loss at 973-1,073 K was due to thermal decomposition of OMS-2 structure with evolution

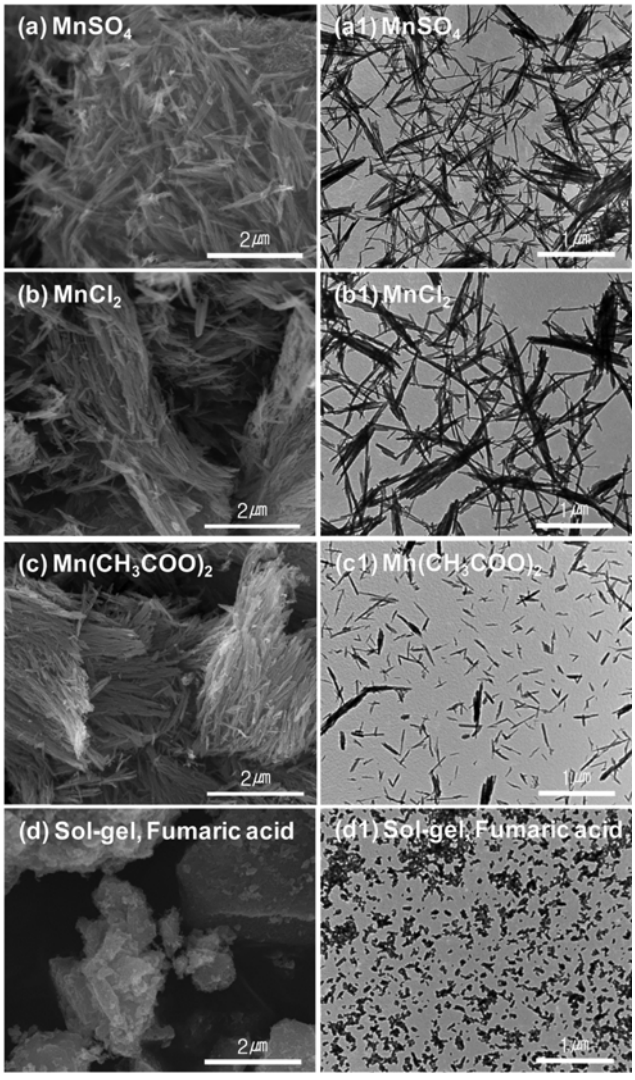

Fig. 2. FE-SEM (a)-(d) and TEM (a1)-(d1) micrographs of OMS-2 adsorbents prepared by oxidation of Mn^{2+} using different precursors; (a), (a1) $MnSO_4$, (b), (b1) $MnCl_2$, (c), (c1) Mn $(CH_3COO)_2$, and by the sol-gel method via (d), (d1) reduction of $KMnO_4$ by fumaric acid.

Table 1. Properties of porous manganese oxide adsorbents prepared by different methods and precursors

Sample	Element composition		Average crystal size (nm)	BET surface area ($m^2\ g^{-1}$)
	K (wt%)	Mn (wt%)		
OMS-2-Ac	4.3	59.1	12.7	110
OMS-2-Sf	4.7	62.0	19.5	104
OMS-2-Cl	4.1	58.8	17.6	77
OMS-2-Sg	4.8	59.4	30.4	57
MnO_2-Fm	-	66.5	27.0	19

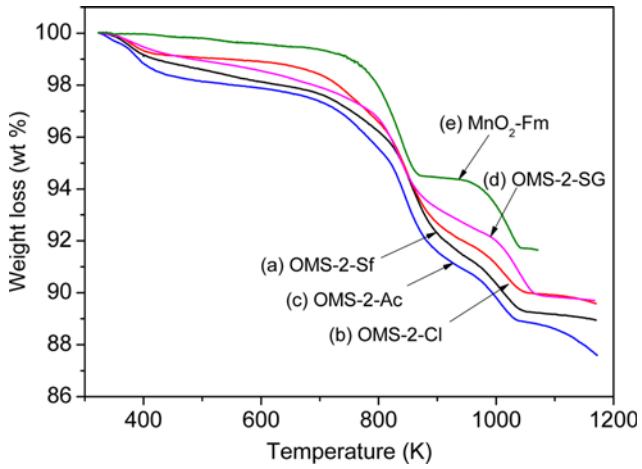

Fig. 3. Thermogravimetric analysis (TGA) results on porous manganese oxide samples prepared by different methods and precursors.

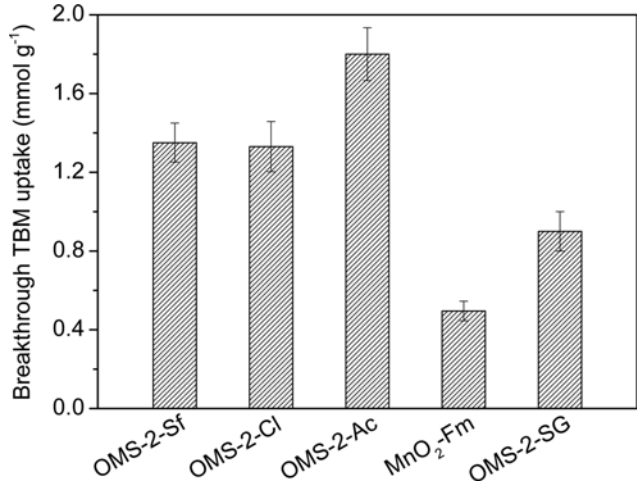

Fig. 4. Breakthrough TBM uptake amount on the porous manganese oxide adsorbents prepared by different methods and Mn precursors.

of lattice oxygen [22]. Fig. 4 shows the breakthrough TBM uptake amounts on the porous manganese oxide adsorbents obtained by different preparation methods and manganese precursors. The TBM uptake on MnO_2-Fm (0.5 mmol g^{-1}) was significantly smaller than those on the OMS-2 adsorbents due to small pore size and surface area that are unfavorable for accommodation of TBM molecules. The OMS-2 adsorbents exhibited TBM uptakes between 0.9 and 1.8 mmol g^{-1} depending on the method used for synthesis and the manganese precursors. Higher breakthrough TBM uptakes were observed on the OMS-2 samples prepared via the Mn^{2+} oxidation (1.4-1.8 mmol g^{-1}) than on OMS-2-Sg obtained by the sol-gel method via $KMnO_4$ reduction (0.9 mmol g^{-1}). A higher TBM adsorption was observed on OMS-2-Ac with a value approximately 130% greater than those on OMS-2-Sf and OMS-2-Cl. Therefore, OMS-2-Ac was chosen for the following studies on the effects of synthesis temperature, time, and Cu doping of OMS-2 for the selective TBM removal.

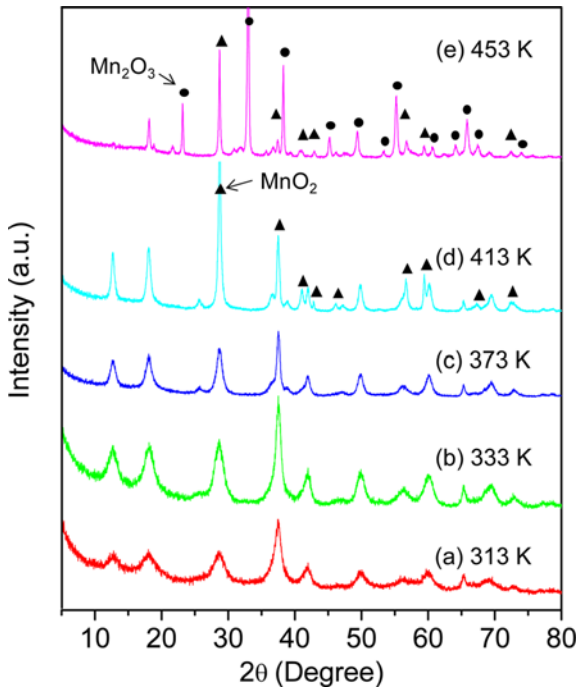

Fig. 5. XRD patterns of OMS-2-Ac samples prepared at various hydrothermal temperatures for 24 h.

2. Effect of Hydrothermal Temperature

OMS-2-Ac adsorbents were prepared at various hydrothermal temperatures between 313 and 453 K for 24 h, and their structures, morphologies, and TBM adsorption properties were investigated. Fig. 5 displays XRD results on these samples. The results clearly indicate that cryptomelane OMS-2 was well developed on the samples prepared between 313 and 373 K. The sample prepared at 413 K exhibited additional diffraction peaks at 28.6, 56.7, and 59.4° indicating considerable formation of pyrolusite MnO_2 structure. On the sample prepared at 453 K, the XRD pattern was largely different, indicating dominant development of Mn_2O_3 crystal structure on this sample prepared at the elevated temperature. Fig. 6 displays FE-SEM (a)-(e) and TEM (a1)-(e1) micrographs on these porous manganese oxide samples prepared at various temperatures. The results demonstrated typical needle-like morphologies of OMS-2 crystallites on the samples prepared between 313 and 413 K. The size of these crystallites increased with hydrothermal temperature in agreement with the XRD results. Crystallite sizes were particularly high on the sample prepared at 413 K, exhibiting densely clustered manganese oxide crystallites, which was likely due to the presence of pyrolusite MnO_2 phase. The sample prepared at 453 K revealed a rod-like morphology of Mn_2O_3 crystallites (several microns in size) that were dominantly formed at this excessively high reaction temperature.

The differences in crystal structures and morphologies of these manganese oxides resulted in considerable differences in their physicochemical and desulfurization properties. Fig. 7 shows TBM breakthrough uptake amounts and BET surface areas of the manganese oxide samples prepared at different synthesis temperatures for 24 h. A decrease in surface area was observed for OMS-2 from 130 to 110 m^2 g^{-1} as the synthesis temperature increased from 333 to 373 K.

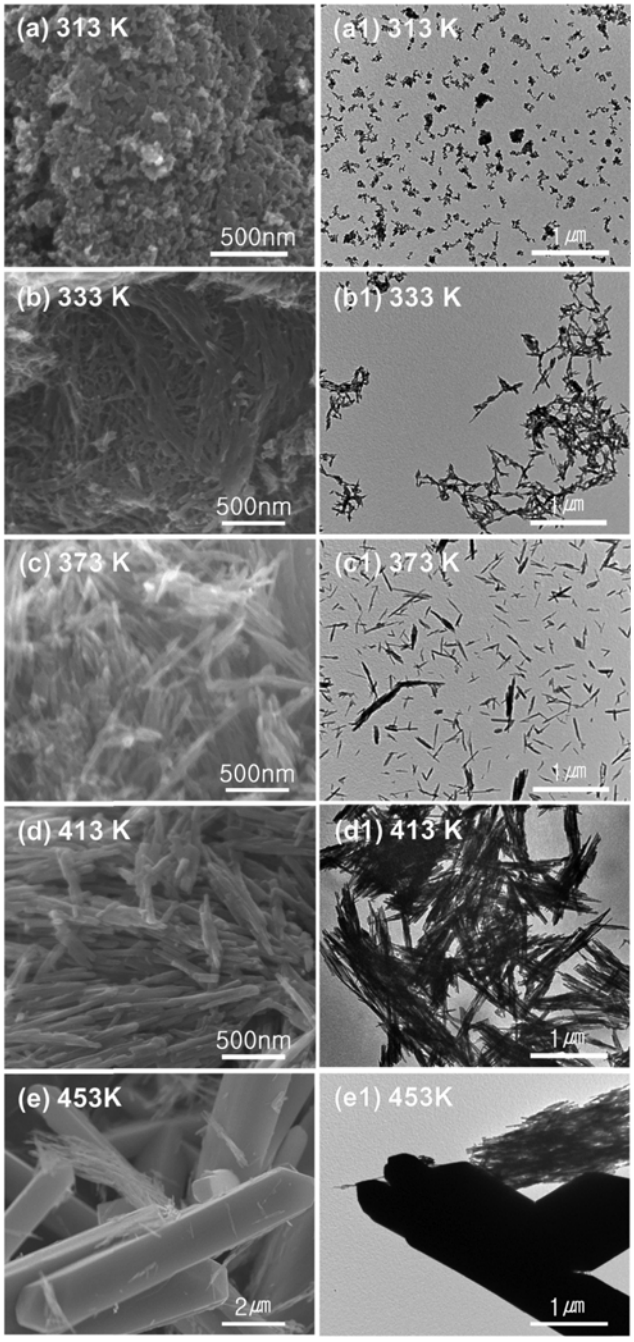

Fig. 6. FE-SEM (a)-(e) and TEM (a1)-(e1) micrographs of porous manganese oxide samples prepared at various temperatures for 24 h.

The surface areas on the samples prepared at 413 and 453 K were particularly small with values of 47 and 5 $m^2 g^{-1}$ due to dominant formation of MnO_2 and Mn_2O_3 crystal phases, respectively. The thermal weight loss of the OMS-2 samples prepared between 313 and 373 K exhibited similar characteristics as determined from TGA analysis, but the extent decreased with temperature, suggesting that crystallinity of OMS-2 was enhanced as the synthesis temperature increased. The weight loss characteristics of the samples prepared at 413 and 453 K were substantially different from those of OMS-2

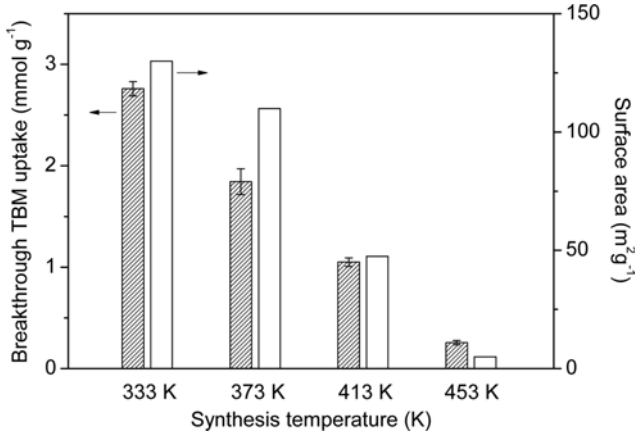

Fig. 7. Breakthrough TBM uptake on OMS-2-Ac adsorbents at different temperature (a) 313 K, (b) 333 K, (c) 373 K, (d) 413 K, and (e) 453 K.

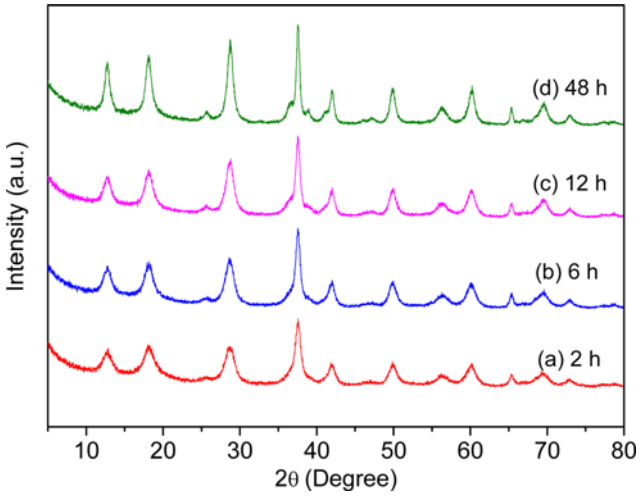

Fig. 8. XRD spectra of OMS-2-Ac samples prepared at 373 K for different synthesis times.

with enhanced thermal stability that reflected substantial formation of MnO_2 and Mn_2O_3 structures at these high temperatures. TBM adsorption on OMS-2 samples exhibited a gradual decrease from 2.8 to 1.9 mmol-S g^{-1} with increasing synthesis temperature from 333 to 373 K. TBM adsorption on the manganese oxides, which consisted mainly of MnO_2 (413 K) and Mn_2O_3 (453 K), were significantly lower than those on the OMS-2 adsorbents.

3. Effect of Hydrothermal Synthesis Time

To investigate the effects of synthesis time for TBM adsorption properties of OMS-2, samples were prepared for various hydrothermal times from 2 to 48 h at 373 K. Fig. 8 shows the XRD results on these samples. It is obvious that cryptomelane OMS-2 was the only and dominant crystal phase on these samples, and its crystallinity increased with hydrothermal synthesis time. The SEM and TEM micrographs for these samples, shown in Fig. 9, agree well with the XRD results. The typical needle-shaped OMS-2 crystallites clustered into bundles could be observed after 2 h of reaction, and their sizes gradually increased with synthesis time.

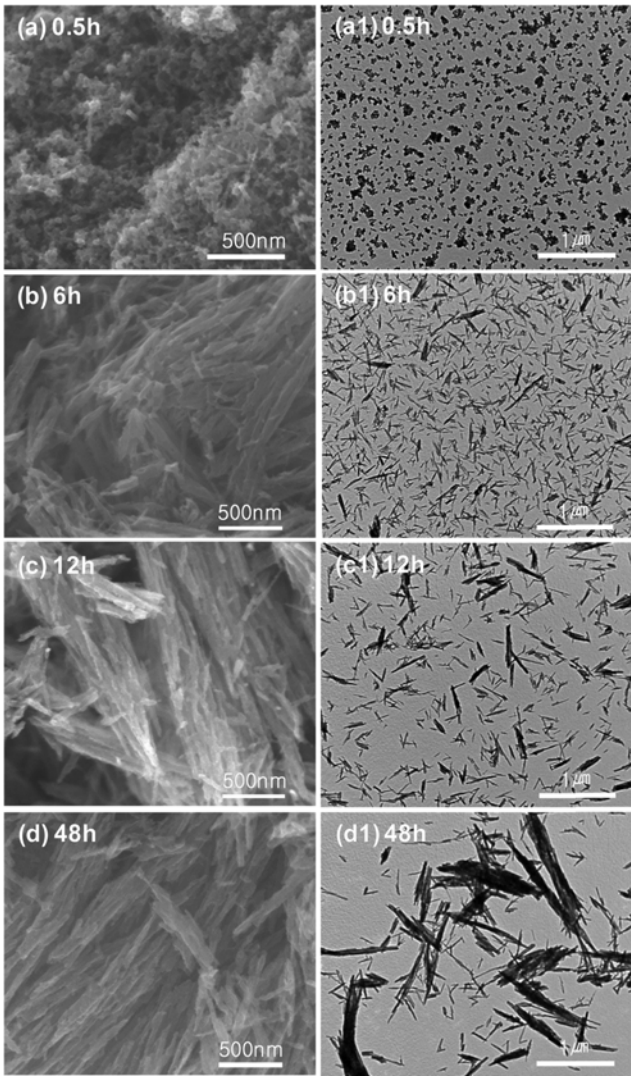

Fig. 9. FE-SEM (a)-(d) and TEM (a1)-(d1) micrographs of OMS-2-Ac samples prepared at 373 K for different synthesis times.

Fig. 10 shows TBM adsorption uptake amounts for these OMS-2 adsorbents. The highest TBM adsorption was obtained on the OMS-2 prepared for 2 h (2.5 mmol g^{-1}) and the value decreased a little to 1.8-1.9 mmol g^{-1} for the rest of the samples prepared for 6-24 h. A lower TBM uptake was observed on the sample prepared for 48 h (1.3 mmol g^{-1}) likely due to its larger crystal size with lower surface area. The high breakthrough TBM uptake on OMS-2 (2.5

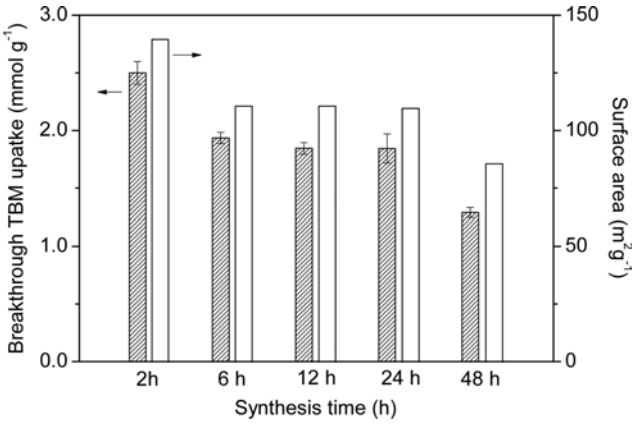

Fig. 10. TBM breakthrough uptake of OMS-2-Ac samples prepared at 373 K for different synthesis times.

mmol g^{-1}, WHSV=0.5) was about 2.6 times higher than NaY (0.95 mmol TBM g^{-1}) and H-β (0.94 mmol TBM g^{-1}, WHSV=5.0) [35], 8.3 times higher than ETS-10 (0.3 mmol TBM g^{-1}, WHSV=1.3) [18], and 11.9 times higher than activated carbon (0.21 mmol TBM g^{-1}, WHSV=2.5) [3]; the TBM feed concentrations in these previous studies are the same at 30 ppm while the weight hourly space velocity (WHSV, ml mg^{-1} min^{-1}) is different as indicated. This considerably high TBM breakthrough uptake on OMS-2 adsorbents suggests their superior applicability for the adsorptive removal of TBM in the fuel desulfurization process for fuel cells.

4. Effect of Copper Dopant

The properties of four different Cu-OMS-2 samples doped with various amounts of Cu were investigated. The samples were designated Cu-OMS-2(1.4), Cu-OMS-2(2.5), Cu-OMS-2(4.8), and Cu-OMS-2(7.8), where the number in the parentheses indicates the amount of copper (wt%) on the samples as determined from elemental analysis. All samples showed similar XRD patterns to that obtained for OMS-2 with no indication of segregated Cu metallic particles on the structure. Table 2 shows elemental compositions, crystal sizes, and surface areas for these samples. The results indicate that an increase in the copper doping level from 1.4 to 7.8 wt% led to an increase in the crystal size of Cu-OMS-2 from 11.9 to 19.5 nm and a slight decrease in BET surface area from 121 to 90 m^2 g^{-1}. The TGA analysis results on these Cu-OMS-2 samples showed similar characteristics to that of OMS-2, indicating that the structure and thermal stability did not vary with the level of Cu doped into the structure. Fig. 11 displays breakthrough TBM adsorption uptake on Cu-OMS-2 samples as a function of Cu doping amounts. The

Table 2. Properties of Cu-OMS-2 adsorbents prepared with different Cu doping level

Materials	Element composition			Average crystal size (nm)	BET surface area (m^2 g^{-1})
	Cu (wt%)	K (wt%)	Mn (wt%)		
OMS-2-Ac	-	4.3	59.1	12.7	110
Cu-OMS-2 (1.4)	1.4	4.3	56.6	11.9	121
Cu-OMS-2 (2.5)	2.5	4.4	56.4	13.1	117
Cu-OMS-2 (4.8)	4.8	4.1	55.0	14.8	97
Cu-OMS-2 (7.8)	7.8	4.0	51.7	19.5	90

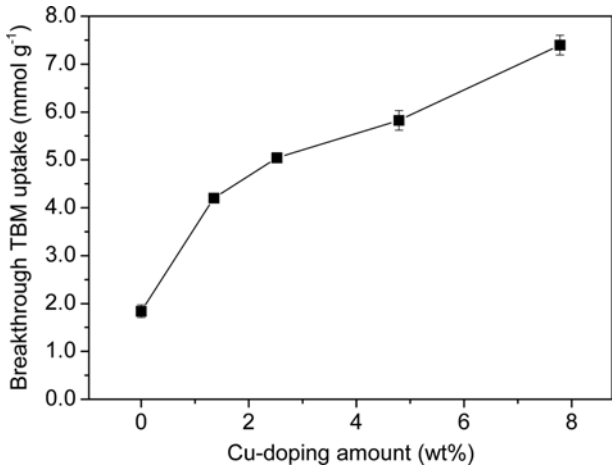

Fig. 11. Breakthrough TBM uptake adsorption amount on Cu-OMS-2 adsorbents as a function of Cu doping amounts. The samples were hydrothermally prepared at 373 K for 24 h.

results indicate that even a small amount of Cu doping (1.4 wt%) in OMS-2 induced a 2.3-times increase in TBM uptake from 1.9 to 4.2 mmol-S g^{-1}. Further increases in the Cu doping amounts in OMS-2 led to gradual increases in TBM uptake amounts, reaching a value of 7.4 mmol-S g^{-1} on Cu-OMS-2 (7.8).

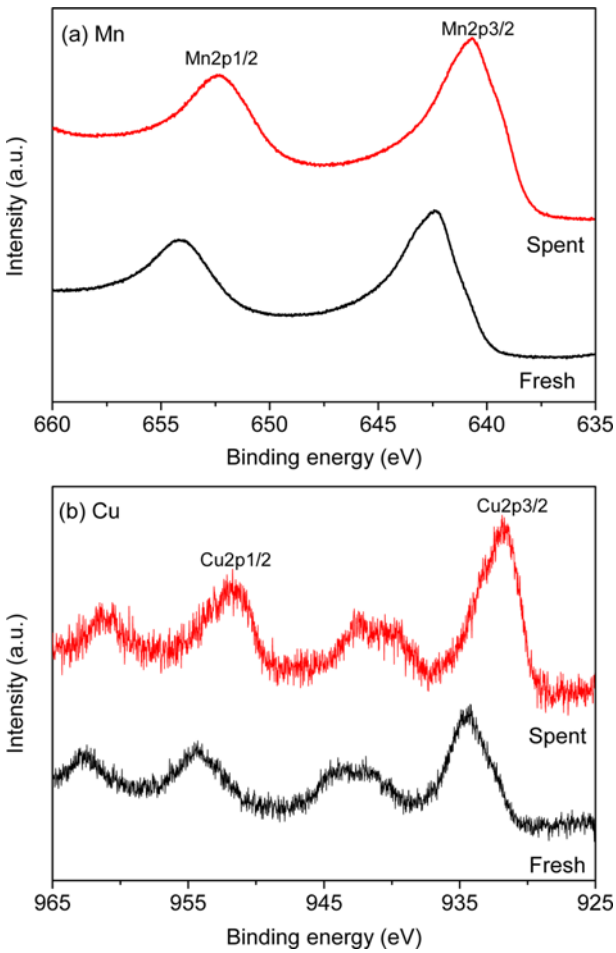

Fig. 12. XPS spectra of the fresh Cu-OMS-2 (4.8) and the spent TBM saturated Cu-OMS-2 (4.8) samples.

Fig. 12 shows the XPS spectra on the fresh and the spent Cu-OMS-2(4.8) samples. The results displayed $Mn2p_{3/2}$ binding energy (BE) for the fresh sample at 642.4 eV, while that for the spent sample was 640.7 eV. The former could be assigned to the BE of Mn^{4+} to lattice oxygen, suggesting that manganese species were present dominantly as Mn^{4+} in the structure, while the latter indicates the existence of Mn-S bonds [36]. It was also confirmed that the $Cu2p_{3/2}$ BE at 933.9 eV was attributed to the Cu-O atomic bonds for the fresh sample, whereas the spent sample showed this BE at 931.9 eV, indicating formation of Cu-S bonds in the structure. The results support the strong adsorptive interactions of TBM with Mn and Cu on the adsorbent surfaces, resulting in the high TBM adsorption capacity and selectivity of OMS-2. The results agree with our previous findings that TBM adsorption on OMS-2 and Cu-OMS-2 is strong and that considerable amounts of residual sulfur could not be removed by simple thermal regeneration [21].

CONCLUSIONS

Porous manganese oxides were prepared by various synthesis methods, precursors, temperatures, and time and investigated for adsorptive removal of TBM from fuel gas. Cryptomelane OMS-2 was formed by oxidation reactions of Mn^{2+} at 373 K when manganese-acetate, -sulfate, and -chloride were utilized as the Mn precursor, and sol-gel method via reduction of $KMnO_4$ by fumaric acid. The type of manganese precursors had significant effects on the OMS-2 crystal growth rate and its formation selectivity. The OMS-2 crystallites developed from manganese sulfate and chloride precursors were larger with enhanced crystallinities than that prepared from manganese acetate at the same synthesis condition. In addition, pyrolusite MnO_2 was formed rather than OMS-2 when manganese formate was used as the precursor, indicating significant contributions from the anion types of the Mn precursors. The oxidation reaction temperature also had significant effects on the formation of OMS-2. The typical OMS-2 crystal structure was well developed between 313 and 373 K, but higher temperatures led to significant formation of the unfavorable MnO_2 and Mn_2O_3 crystal phases. A considerably high breakthrough TBM uptake of 2.5 mmol g^{-1} was obtained for OMS-2, which is greater than previously reported values for activated carbon, zeolite, and porous metal oxide based solid adsorbents. Copper dopants in Cu-OMS-2 played significant roles exhibiting a gradual enhancement in TBM adsorption amounts with increasing Cu doping level. A markedly high TBM adsorption (7.4 mmol g^{-1}) was obtained for Cu-OMS-2 containing 7.8 wt% Cu. The XPS studies revealed sulfidation of the adsorbents due to strong bonding of sulfur species with the Mn and Cu species on the structure, which is in good agreement with the low thermal regenerability of OMS-2 adsorbents as reported in our previous work.

ACKNOWLEDGEMENTS

H. C. Woo acknowledges the support by Basic Science Research Program through the National Research Foundation of Korea funded

by the Ministry of Education (C-D-2014-0807). D. Lee acknowledges financial support from the Korea Research Foundation (Grant 2014-R1A1A2053895).

REFERENCES

1. D. Lee, J. Kim, H. C. Lee, K. H. Lee, E. D. Park and H.-C. Woo, *J. Phys. Chem. C*, **112**, 18955 (2008).
2. S. Satokawa, Y. Kobayashi and H. Fujiki, *Appl. Catal. B: Environ.*, **56**, 51 (2005).
3. P. H. Ho, S.-Y. Lee, D. Lee and H.-C. Woo, *Int. J. Hydrogen Energy*, **39**, 6737 (2014).
4. C. Song, *Catal. Today*, **77**, 17 (2002).
5. R. Ferrauto, S. Hwang, L. Shore, W. Ruettinger, J. Lampert, T. Giroux, Y. Liu and O. Ilinich, *Annu. Rev. Mater. Res.*, **33**, 1 (2003).
6. D. D. Whitehurst, T. Isoda and I. Mochida, *Adv. Catal.*, **42**, 345 (1998).
7. H. Cui and S. Q. Turn, *Appl. Catal. B: Environ.*, **88**, 25 (2009).
8. H. Tamai, H. Nagoya and T. Shiono, *J. Colloid Interface Sci.*, **300**, 814 (2006).
9. S. Hernandez, L. Solarino, G. Orsello, N. Russo, D. Fino and G. Saracco, *Int. J. Hydrogen Energy*, **33**, 3209 (2008).
10. D. Lee, E.-Y. Ko, H. C. Lee, S. Kim and E. D. Park, *Appl. Catal. A: Gen.*, **334**, 129 (2008).
11. Y. H. Kim, H. C. Woo, D. Lee, H. C. Lee and E. D. Park, *Korean J. Chem. Eng.*, **26**, 1291 (2010).
12. C.-L. Hwang and N.-H. Tai, *Appl. Catal. B: Environ.*, **93**, 363 (2010).
13. A. S. H. Salem, *Ind. Eng. Chem. Res.*, **33**, 336 (1994).
14. R. T. Yang, A. J. Hernández-Maldonado and F. H. Yang, *Science*, **301**, 79 (2003).
15. F. T. T. Ng, A. Rahman, T. Ohasi and M. Jiang, *Appl. Catal. B: Environ.*, **56**, 127 (2005).
16. C. L. Garcia and J. A. Lercher, *J. Phys. Chem.*, **95**, 10729 (1991).
17. S. Velu, X. Ma and C. Song, *Ind. Eng. Chem. Res.*, **42**, 5293 (2003).
18. G. S. Jung, D. H. Park, D. H. Lee, H. C. Lee, S. B. Hong and H. C. Woo, *Appl. Catal. B: Environ.*, **100**, 264 (2010).
19. H.-T. Kim, S.-M. Kim, K.-W. Jun, Y.-S. Yoon and J.-H. Kim, *Int. J. Hydrogen Energy*, **32**, 3603 (2007).
20. P. Jeevanandam, K. J. Klabunde and S. H. Tetzler, *Micropor. Mesopor. Mater.*, **79**, 101 (2005).
21. P. H. Ho, S. Y. Lee, J. Kim, D. Lee and H. C. Woo, *Fuel Process. Technol.*, **131**, 238 (2015).
22. G. Qiu, H. Huang, S. Dharmarathna, E. Benbow, L. Stafford and S. L. Suib, *Chem. Mater.*, **23**, 3892 (2011).
23. E. K. Nyutu, C.-H. Chen, S. Sithambaram, V. M. B. Crisostomo and S. L. Suib, *J. Phys. Chem. C*, **112**, 6786 (2008).
24. N. N. Opembe, C. K. King'ondu, A. E. Espinal, C.-H. Chen, E. K. Nyutu, V. M. Crisostomo and S. L. Suib, *J. Phys. Chem. C*, **114**, 14417 (2010).
25. Q. Feng, H. Kanoh, Y. Miyai and K. Ooi, *Chem. Mater.*, **7**, 148, (1995).
26. H. C. Genuino, S. Dharmarathna, E. C. Njagi, M. C. Mei and S. L. Suib, *J. Phys. Chem. C*, **116**, 12066 (2012).
27. W. Y. Hernández, M. A. Centeno, S. Ivanova, P. Eloy, E. M. Gaigneaux and J. A. Odriozola, *Appl. Catal. B: Environ.*, **123**, 27 (2012).
28. R. Kumar, S. Sithambaram and S. L. Suib, *J. Catal.*, **262**, 304 (2009).
29. T. Oishi, K. Yamaguchi and N. Mizuno, *ACS Catal.*, **1**, 1351 (2011).
30. O. Ghodbane, F. Ataherian, N.-L. Wu and F. Favier, *J. Power Sources*, **206**, 454 (2012).
31. C. H. Jiang, S. X. Dou, H. K. Liu, M. Ichihara and H. S. Zhou, *J. Power Sources*, **172**, 410 (2007).
32. J. Yuan, X. Liu, O. Akbulut, J. Hu, S. L. Suib, J. Kong and F. Stellacci, *Nat. Nano.*, **3**, 332 (2008).
33. S. Ching, J. L. Roark, N. Duan and S. L. Suib, *Chem. Mater.*, **9**, 750 (1997).
34. X. F. Shen, Y. S. Ding, J. Liu, J. Cai, K. Laubernds, R. P. Zerger, A. Vasiliev, M. Aindow and S. L. Suib, *Adv. Mater.*, **17**, 805 (2005).
35. H. Wakita, Y. Tachibana and M. Hosaka, *Micropor. Mesopor. Mater.*, **46**, 237 (2001).
36. J. F. Moulder, W. F. Stickle, P. E. Sobol, K. D. Bomben, J. Chastain and R. C. King, *Handbook of X-ray Photoelectron Spectroscopy*, Physical Electronic, U.S.A. (1995).